Single Magnetic Particle Motion in Magnetomotive Ultrasound: An Analytical Model and Experimental Validation

Benjamin E. Levy and Amy L. Oldenburg

***Abstract*—Magnetomotive Ultrasound (MMUS) is an emerging imaging modality in which magnetic nanoparticles (MNPs) are used as contrast agents. MNPs are driven by a time-varying magnetic force, and the resulting movement of the surrounding tissue is detected with a signal processing algorithm. However, there is currently no analytical model to quantitatively predict this magnetically-induced displacement. Toward the goal of predicting motion due to forces on a distribution of MNPs, in this work a model originally derived from the Navier-Stokes equation for the motion of a single magnetic particle subject to a magnetic gradient force is presented and validated. Displacement amplitudes for a spatially inhomogeneous and temporally sinusoidal force were measured as a function of force amplitude and Young's modulus, and the predicted linear and inverse relationships were confirmed in gelatin phantoms respectively with 3 out of 4 datasets exhibiting $R^2 \geq 0.88$. The mean absolute uncertainty between the predicted displacement magnitude and experimental results was 14%. These findings provide a means by which the performance of MMUS systems may be predicted to verify that systems are working to theoretical limits, and to compare results across laboratories.**

***Index Terms*—Contrast-enhanced ultrasound, magnetomotive ultrasound (MMUS), elastic media**

I. INTRODUCTION

MAGNETOMOTIVE ultrasound (MMUS) is a contrast-enhanced imaging modality that uses magnetic nanoparticles (MNPs) as contrast agents[1]. Magnetomotive imaging, first developed by Oldenburg *et al.* for optics in 2005[2], and first deployed in ultrasound by Oh *et al.* in 2006[3], utilizes a time-varying magnetic force to drive MNPs, and a signal processing algorithm to detect them. Magnetically modulated MNPs embedded in the imaging area induce motion in the surrounding medium to which they are mechanically coupled. Though ultrasound cannot directly resolve MNPs due to resolution constraints and low echogenicity, contrast to distributions of MNPs is achieved through the identification of areas of the medium exhibiting magnetically-induced motion. Image processing approaches such as a frequency- and phase-locking (FPL) algorithm may be used to identify such areas[4]. MMUS has shown promise toward applications such as imaging of sentinel lymph nodes, as demonstrated in rats[5], imaging carcinoma, as demonstrated in mice[6], colorectal cancer staging[7], magnetic drug targeting[8], and thrombosis imaging[9]. However, to date no model is available to predict both the absolute magnitude and functional dependencies of magnetically-induced motion for any given set of imaging system and target parameters. In order to make cross-system comparisons easier and to aid in system design, an analytical model robust to a spatially inhomogeneous magnetic force is proposed and experimentally validated. Direct measurements of the magnetic force were made using a force sensing pendulum, which lead to precise theoretical predictions.

A variety of hardware, contrast agent, and medium-specific parameters may affect the magnetically-induced motion for a given MMUS experiment. For example, a wide range of magnetic force delivery techniques are currently under study. Approaches include supplying time-varying current waveforms to electromagnets in order to produce sinusoidal[4], [10] pulsed[11], [12] or coded[8] forces, a scheme derived from magnetic particle imaging (MPI) in which a strong static gradient field is superposed on a weaker sinusoidally modulated magnetic field[13], and even a rotating permanent magnet[14]. Characteristics of these forces such as frequency and amplitude have been shown to affect MMUS signal[15], [16], and in the usual case where the force field is spatially inhomogeneous, areas of higher magnetic force correspond to greater MNP motion[17]. The choice of contrast agent can also significantly affect results, as MNP concentration[4], [12], [17], [18], size[19], and coating[20] have all been shown to correlate with differences in detected motion. Furthermore, research in this group[9] and others[7], [21] has shown imaging to be sensitive to medium properties such as Young's modulus.

Without a model capable of predicting the effects of the parameters described above, challenges arise in designing and optimizing MMUS systems to ensure they are performing as intended. Furthermore, given the many variables present in the production of an MMUS image, cross-system comparisons are challenging. As an example, Evertsson *et al.'s* MMUS system[18] produces displacements approximately 12.5 times larger than those generated by the apparatus used in this work[9], but the underlying reasons are complex. The tip of Evertsson's electromagnet core was placed significantly closer to the imaging area than the two cores in this group's system,

Manuscript received February 17, 2021; accepted April 9, 2021. Date of publication XXX XX, 2021; date of current version XXX XX, 2021. This work was supported in part by the National Institutes of Health under grant R21 HL 119928, and by the Department of Defense Air Force Office of Scientific Research under grant FA9550-14-1-0208.

B. E. Levy is with the Department of Physics and Astronomy, University of North Carolina, Chapel Hill, NC 27599 USA (email: levyb@unc.edu).

A. L. Oldenburg is with the Department of Physics and Astronomy, and also with the Biomedical Research Imaging Center, University of North Carolina, Chapel Hill, NC 27599 USA (email: aold@physics.unc.edu).

Digital Object Identifier XXXX

and the Young's modulus of the phantom was lower, both of which would likely lead to higher displacements. However, Evertsson used MNPs at a lower iron concentration which may lower displacement amplitudes, and they also used polyethylene glycol-coated MNPs with $Fe^{(II,III)}{}_3O_4$ (magnetite) cores while this group used $Fe^{(II,III)}{}_3O_4$ nanopowder with no coating. The consequences of these differences are challenging to predict. To date, finite element simulations have been used to qualitatively predict displacements[17] and as part of an iterative approach to quantitatively predict MNP distributions from MMUS data[22]. More recently a displacement model was used to characterize the nonlinear force on MNPs up to a scaling factor which had to be determined experimentally[23]. A model capable of quantitative displacement predictions would reveal the variables with the highest impacts on imaging and aid in cross-lab comparisons when using different phantom materials, magnet geometries, and excitation schemes.

In this work, an analytical model for the magnetically-induced motion of a single particle embedded in a soft tissue-like medium and subject to an MMUS driving force is presented. Motion of MNPs may be tracked with a variety of schemes such as FPL[4], [10], [24], cross-correlation methods[8], [11], blind source separation[25] and other approaches[26]. In this work a sinusoidal driving force is assumed and *MMUS signal* is defined as the magnetically-induced vibration amplitude, the quantity estimated by the FPL algorithm. Thus, the model is designed to predict displacement amplitudes to match. However, the approach presented in this work could be adapted for any MMUS system employing a driving force of sufficiently low frequency (~1 Hz) that viscoelastic effects may be ignored[27], and for which image processing is displacement-based. As a first step toward a full model of MMUS signal generation for arbitrary distributions of MNPs in media with complicated boundary conditions, the model presented here, based on the Navier-Stokes equation under the assumptions of an incompressible fluid with a low Reynolds number, accounts for the motion of a single magnetic particle in an infinite homogeneous, linearly-elastic, and isotropic medium, subject to a spatially inhomogeneous and temporally sinusoidal magnetic driving force. Then using phantoms, the model's ability to predict the absolute magnitude and functional dependence of MMUS signal for media of different Young's moduli and at different force amplitudes and locations within the inhomogeneous force field is validated. In order to generate a precise magnetic force map for validation, a force-sensing pendulum was constructed capable of direct, spatially-resolved force measurements without relying on an estimate of the magnetic susceptibility of the MNPs, which is challenging to do accurately. Study results demonstrate the potential for an MMUS signal generation model to allow for easier system design and cross-platform comparisons. Further development could lead to the ability for MMUS to sense medium properties while controlling for the particles used, the magnetic delivery scheme, and imaging parameters.

II. Theory

This analytical model is designed to predict the displacement as a function of time for a uniform ball (*i.e.*, a solid sphere) with linear magnetization embedded with a no-slip boundary condition in an infinite, homogeneous, linear-elastic, and isotropic medium with a Young's modulus much less than that of the ball, subject to a temporally-sinusoidal but spatially inhomogeneous magnetic driving force. Displacement as a function of force magnitude and frequency, ball radius, ball and medium mass density, and medium elastic modulus will then be extracted and experimentally validated as described in Sec. III.

A solution with two terms is expected. A steady-state sinusoidal term will dominate at long times after the force is first applied, and a transient "ring-down" term may potentially complicate the extraction of the MMUS signal by dominating at short times. Understanding the time scale associated with the transient term will allow for the exclusion of data collected before the steady-state behavior dominates, or the selection of imaging parameters that make this behavior negligible.

In order to derive the analytical model, the MMUS driving force will be convolved with the medium impulse response via the following steps. First the driving force will be Fourier transformed into the frequency domain. Then the frequency domain force and impulse response will be multiplied to arrive at the frequency domain displacement. Finally, this displacement will be transformed back into the time domain.

The magnetic driving force,

$$f(t) = \theta(t)\, a\, (1-\cos(\omega_0 t)), \tag{1}$$

is sinusoidal with driving frequency ω_0 and force amplitude a. As shown by the dashed magenta trace in Fig. 1a, the sinusoid is offset such that the maximum force is $2a$, and the minimum force is 0, consistent with our system which employs an electromagnet driven by a unipolar power supply. The Heaviside step function $\theta(t)$ accounts for the force being switched on at $t = 0$. Convolution between the Fourier transforms of $\theta(t)$ and $g(t) = a(1-\cos(\omega_0 t))$ gives

$$F(\omega) = (1/2\pi)\Theta(\omega) * G(\omega), \tag{2}$$

where $F(\omega)$ is the transform of (1), $\Theta(\omega) = \pi\delta(\omega) + i/\omega$, and $G(\omega) = \pi\, a\,(2\delta(\omega) - \delta(\omega+\omega_0) - \delta(\omega-\omega_0))$. In these expressions δ is the Dirac delta function, and i is the unit imaginary number. Equation (2) then simplifies to

$$F(\omega) = a\pi\left[\delta(\omega) - \frac{\delta(\omega+\omega_0)}{2} - \frac{\delta(\omega-\omega_0)}{2}\right] - \frac{ai\omega_0^2}{\omega^3 - \omega\omega_0^2}. \tag{3}$$

The first term in this expression contributes only to the steady-state behavior of the solution, while the second term contributes to both the steady-state and transient behaviors.

By solving the continuity and Navier-Stokes equations under the assumptions of an incompressible fluid (medium) with a low Reynolds number, the impulse response $H(\omega)$ of the medium may be determined by following the derivation in Ilinskii *et al.*[28] in which the expression

$$\begin{aligned} F(\omega) = \; & -\left[\frac{4}{3}\pi R^3 \rho_b\right]\omega^2 U(\omega) \\ & + 6\pi\mu R\left[1 - ik(\omega)R - \frac{1}{9}k(\omega)^2 R^2\right]U(\omega) \end{aligned} \tag{4}$$

relates the frequency domain displacement $U(\omega)$ to the frequency domain force acting on a rigid sphere in a

homogeneous viscoelastic medium. In (4) R and ρ_b are the ball radius and density, respectively, while μ and ρ are the medium shear modulus and density, respectively. The quantity

$$k(\omega)^2 \equiv \frac{\omega^2 \rho}{G' - iG''} \tag{5}$$

is the square of the complex wavenumber, where $G' = \mu$ is the medium shear storage modulus, and G'' is the shear loss modulus which may also be written in terms of the dynamic viscosity as $\omega\eta$. Because G'' is much smaller than G' for the gels in this experiment at the 2 Hz frequency used[29], (5) may be simplified to $k(\omega) = \omega(\rho/\mu)^{1/2}$. Importantly, it has been shown that soft tissues exhibit the somewhat universal property $G'' \approx 0.1G'$ for frequencies around 1 Hz, implying that biological relevance is not lost with this simplification[27]. By the convolution theorem, the frequency domain displacement is

$$U(\omega) = H(\omega)F(\omega). \tag{6}$$

Thus dividing both sides of (4) by $U(\omega)$ yields

$$H(\omega) = \left(6\pi\mu R\left[1 - ik(\omega)R - \tfrac{1}{9}k(\omega)^2R^2\right] - \tfrac{4\pi}{3}R^3\rho_b\omega^2\right)^{-1}, \tag{7}$$

which describes the displacement associated with an impulse force. The product of (7) and (3) is

$$U(\omega) = a\pi H(\omega)\left[\delta(\omega) - \frac{\delta(\omega+\omega_0)}{2} - \frac{\delta(\omega-\omega_0)}{2}\right] - \frac{ai\omega_0^2 H(\omega)}{\left(\omega^3 - \omega\omega_0^2\right)}, \tag{8}$$

the ball displacement due to the sinusoidal MMUS force.

To obtain the time-domain displacement, an inverse Fourier transform of (8) is needed. By making use of the Dirac delta function identity three times, the first term may be simplified to form half of the steady state solution. The second term leads to a complex integral with five poles, so simplification requires contour integration as well as both the Cauchy residue theorem and Jordan's lemma. The result is the other half of the steady state solution and all of the transient solution. The sum of these contributions yields the time domain displacement for t > 0,

$$u(t) = S\left[1 - \frac{1}{\sqrt{\chi^2+\psi^2}}\cos\left(\omega_0 t - \phi_s\right) + \omega_0^2 e^{-\omega_b t}\frac{\sqrt{Z^2+1}}{\sqrt{X^2+Y^2}}\cos\left(\omega_a t - \phi_t\right)\right], \tag{9}$$

in which sinusoidal motion at the driving frequency ω_0 (steady-state) is superposed with an exponentially decaying, sinusoidal term at another frequency ω_a (transient). The first term is centered at the positive displacement offset

$$S = a / 6\pi\mu R \tag{10}$$

and oscillates with amplitude $S(\chi^2 + \psi^2)^{-1/2}$, where

$$\chi = 1 - \frac{1}{9}\frac{\rho}{\mu}\omega_0^2 R^2\left(1 + 2\frac{\rho_b}{\rho}\right), \quad \text{and} \quad \psi = \omega_0 R\sqrt{\frac{\rho}{\mu}}. \tag{11}$$

By setting the first derivative with respect to ω_0 of (9) equal to zero and solving the resulting expression appropriately, the peak (or resonant) frequency

$$\omega_{res} = \frac{3}{R}\frac{\sqrt{2(\rho_b/\rho) - 7/2}}{1 + 2(\rho_b/\rho)}\sqrt{\frac{\mu}{\rho}}, \tag{12}$$

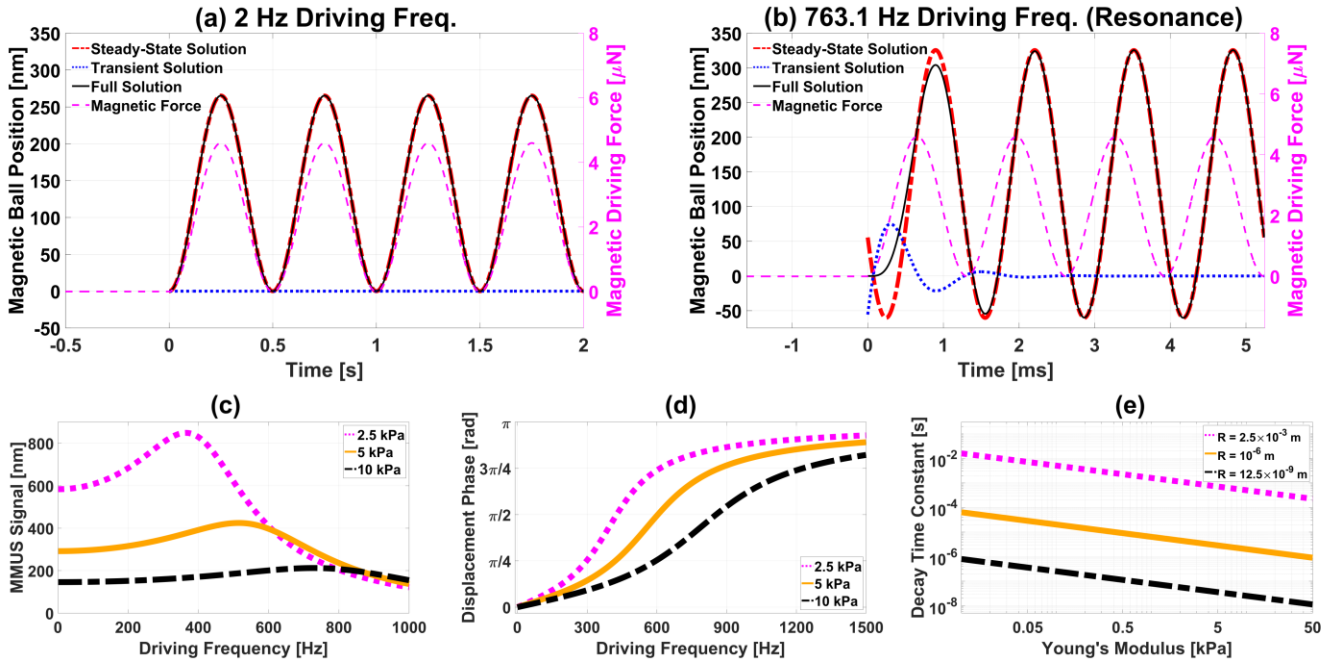

Fig. 1. Magnetic ball position as a function of time as predicted by (9) for (a) 2 Hz (used in this study) and (b) 763.1 Hz (resonant) magnetic driving frequency with a force amplitude of a = 2.3 μN. In each case the sinusoidal force is displayed as a dashed magenta line, while the model prediction is a solid black line. The dot-dashed red and dotted blue lines represent the steady-state and transient parts of the solution, respectively. Constants in (9) were set to match parameters realized in this work. The medium Young's modulus was 11 kPa with a quasi-incompressible Poisson's ratio of 0.495 and a density of 1017 kg/m^3, while the ball radius and density were 0.25 mm and 7850 kg/m^3, respectively to match the chrome steel ball bearings used for validation. The steady-state MMUS signal (magnetically-induced displacement amplitude) and displacement phase relative to the driving force are presented in (c) and (d) as a function of driving frequency. Traces are displayed for three different Young's moduli in each plot, while all other constants are maintained. The resonant frequency is visible as the peak in displacement amplitude as well as the π/2 crossing on the phase plot. The exponential decay time constant in the transient term as a function of Young's modulus is shown in (e). Results are given for three different ball radii (the magnetic ball, a micro-bead, and a typical nanoparticle) while all other constants are unchanged. This demonstrates that the transient term only becomes relevant when the driving frequency is high, the ball radius is large, or the stiffness of the medium is low.

may be obtained. Fig. 1 depicts the steady-state solution as a red dot-dashed line for the low frequency (a) and resonant frequency (b) cases. As shown in Fig. 1a, in the low frequency limit where $\omega_0 \ll \omega_{res}$, the denominator $(\chi^2 + \psi^2)^{-1/2} \approx 1$, which yields a displacement amplitude equal to the central offset value S. Thus the ball position varies between 0 and $2S$. However, higher driving frequencies lead to amplitudes that differ from S as shown in Fig. 1c. Displacement amplitudes increase to resonance, and then decay when $\omega_0 > \omega_{res.}$ The steady-state term's phase lag relative to the driving force

$$\phi_s = \tan^{-1}(\psi / \chi), \tag{13}$$

is less than 0.01 radians when $\omega_0 \ll \omega_{res}$, but as shown in Fig. 1d, increases to $\pi/2$ at resonance, and then asymptotes to π as ω_0 goes to infinity. The larger displacement amplitude and $\pi/2$ phase lag are clearly visible in Fig. 1b despite the same driving force. Thus it becomes clear that by keeping magnetic driving frequencies in the tens of Hz range or lower as was done in this study, the steady-state solution may be assumed to be a simple cosine with a positive vertical offset equal to its amplitude and zero phase lag relative to the driving force.

The transient term consists of a cosine of frequency

$$\omega_a = \frac{3}{2R}\frac{\sqrt{8(\rho_b/\rho)-5}}{1+2(\rho_b/\rho)}\sqrt{\frac{\mu}{\rho}} \tag{14}$$

multiplied by a decaying exponential with decay constant

$$\omega_b = \frac{9}{2R}\frac{1}{1+2(\rho_b/\rho)}\sqrt{\frac{\mu}{\rho}}. \tag{15}$$

The following combinations of (14) and (15),

$$\begin{aligned} X &= \omega_a^2 - \omega_b^2 - \omega_0^2 \\ Y &= 2\omega_a\omega_b \\ Z &= \omega_b / \omega_a \end{aligned} \tag{16}$$

are used to provide an overall scaling factor, and to define the transient term phase lag,

$$\phi_t = \tan^{-1}\left(\frac{Y+ZX}{X-ZY}\right), \tag{17}$$

relative to the driving force. Note that, as shown in Fig. 1e, the exponential decay time constant $1/\omega_b$ is much shorter than the period of the magnetic driving force for relevant medium, ball, and excitation frequency parameters, indicating that the transient behavior may be ignored. However, systems operating at higher frequencies approaching ω_b may be affected by this transient term as shown by the blue dotted trace in Fig. 1b. In such cases, the transient frequency given in (14) becomes relevant. This frequency is dependent only on medium and ball parameters, and is in the range of thousands of rad/s and above for all realizable parameters. For example, as R decreases toward the nanoparticle regime, the magnitude of the transient term decreases several orders of magnitude below that of the steady-state term, and the decay time constant drops to the μs range or less. Ultimately, in the $\omega_0 \ll \omega_{res}$ limit explored in this work, (9) may be approximated as

$$u(t) = \frac{a}{6\pi\mu R}\left[1-\cos(\omega_0 t)\right] = \frac{a(1+\nu)}{3\pi E R}\left[1-\cos(\omega_0 t)\right], \tag{18}$$

where in the 2nd equality, μ has been replaced by the medium Young's modulus E and Poisson's ratio ν. The factor outside of the square brackets, S, is the MMUS signal validated in Sec. III.

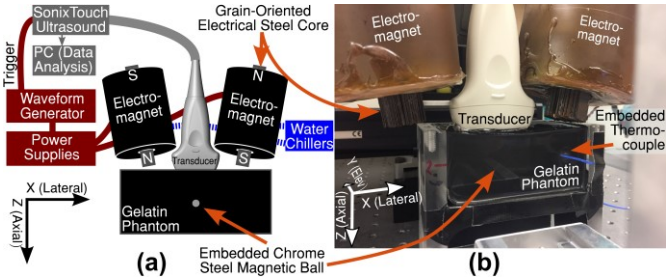

Fig. 2. Schematic diagram (a) and photograph (b) of the open-air MMUS system utilized in this study.

III. Validation Methods

A. Open-Air Magnetomotive Ultrasound System

The MMUS imaging apparatus described in Levy *et al.*[9] was used for this work. Briefly, imaging was conducted with an Ultrasonix SonixTouch platform and an L14-5/38 transducer (Analogic Corporation, Peabody, MA, USA) decreased to a 1 MHz transmit and receive frequency to provide coarser resolution for this study as discussed in Sec. V-B, and focal depths between 10 and 20 mm. With these parameters, the axial resolution was 0.8 mm, and the lateral resolution ranged from 1.1 to 2.2 mm at the focus. Thus the 0.5 mm diameter imaging targets discussed in Sec. III-B were sub-resolution. Beamformed RF data was transferred to a separate PC for offline processing in MATLAB R2020a (Mathworks Inc, Natick, MA, USA). As shown in Fig. 2 the transducer was positioned between the two water cooled solenoid electromagnets in a configuration that allowed for samples of arbitrary volume to be imaged. An Agilent 33522A arbitrary waveform generator (Keysight Technologies, Santa Rosa, CA, USA) created a current waveform in each of the electromagnets via two Kepco ATE-75-15M, 1000 W power supplies (Kepco Inc, Flushing, NY, USA). This resulted in a magnetic gradient of ~0.02 T^2/m in the imaging area. The flow system described in Levy *et al.*[9] was removed for this work.

MMUS images were generated in the same manner as described in previous work[9]. Two 7.5 s stacks of beamformed RF data were collected at 61.667 fps, the first with the magnets turned off to allow for background subtraction, and the second with their current modulated square-root sinusoidally at 1.9891 Hz, a value chosen to minimize discrete Fourier transform errors. This led to a sinusoidal magnetic driving force of the same frequency. The FPL algorithm[4] was then used to identify regions of the image containing motion at the same frequency as and in phase with the magnetic driving force, and to determine the amplitude of that motion. Pixels with corresponding B-mode intensities less than 40% of the mean B-mode intensity were excluded for phase noise suppression. Resulting MMUS images are displayed with magnetically-induced displacement amplitude (*MMUS Signal*) given in nanometers. A median filter with a box size equivalent to one resolution cell was used for display purposes only.

B. Phantom Preparation

Gelatin tissue-mimicking phantoms with one or more embedded sub-resolution magnetic balls were created with physiologically relevant Young's modulus, acoustic attenuation, and speed of sound values for soft tissue in the 5×10×5 cm (axial × lateral × elevational) rectangular acrylic phantom mold shown in Fig. 2b. Gelatin was poured into the mold via the open top. To avoid imaging through boundaries between gelatin layers, an acrylic side was then removed, the phantom was rotated, and imaging was conducted via this perpendicular face. The interior of the removable side was coated in non-stick cooking spray for easy release.

Phantoms were prepared in three steps: first a base layer of gelatin was poured into the mold and allowed to gel, second a magnetic ball was placed on top and covered with a thin layer of gelatin, and finally a top layer was poured. For the base layer, nominally 10 kPa Young's modulus graphite-infused gelatin was prepared as described in Levy *et al.*[9] based on a formulation first published by Madsen *et al.*[30] Gelatin from porcine skin (4.5 wt%), synthetic graphite nanopowder (4.4 wt%), and n-propanol (3.0 wt%), were combined to make 250 ml of gelatin solution, and cooled to 28°C. After a minute of gentle stirring, the solution was poured into the phantom mold until it was approximately two-thirds full. The phantom was placed on ice in the refrigerator with a thermocouple embedded to monitor its temperature. The remaining gelatin solution was quickly returned to the hot plate where stirring resumed, and the temperature was increased to 40°C.

Once the gelatin temperature in the mold reached 18°C, the phantom was removed from the refrigerator and the top surface was heated for 5-10 seconds with a heat gun in order to prevent air pockets from forming between layers. For phantom 1, a 0.5 mm diameter chrome steel ball bearing (Salem Specialty Ball, Inc, Canton, CT, USA) was placed onto the gelatin and 2 ml of heated gelatin solution from the beaker was pipetted on top of the ball. For phantom 2, three balls were positioned so as to experience different amounts of magnetic gradient force within the MMUS system's field-of-view. The beaker containing the remaining heated gelatin was returned to the ice bath and cooled to 28°C. After briefly applying the heat gun to the solidified top surface of the phantom, this gelatin was added until the phantom mold was full. The phantom was placed on ice in the refrigerator, and once its internal temperature reached 18°C, it was wrapped in plastic for overnight refrigeration.

C. Calibration of Phantom Temperature to Young's Modulus

The Young's modulus of gelatin varies with temperature. Therefore, images collected as a phantom warmed from refrigerator temperature to room temperature allowed for the expedient study of MMUS displacement amplitudes as a function of Young's modulus. In order to phenomenologically determine the functional relationship between temperature and Young's modulus, the following procedure was performed.

Four graphite-infused gelatin cylinders were created using the same recipe described in Sec. III-B. The cylinders were created in 6.1 cm diameter PVC molds and were between 3.0 and 3.5 cm tall for a total volume of about 100 ml. The sides of the molds were coated with nonstick cooking spray for easy release, and a thermocouple was embedded such that the wire emerged from the curved edge of the gelatin cylinder leaving the two flat faces uninterrupted. Care was taken to ensure that the distance of the thermocouple from the surface in these cylinders was approximately the same as in Phantoms 1 and 2.

After overnight refrigeration, the gelatin cylinders were removed the following morning, and immediately subjected to compression testing with a TA.XT Plus texture analyzer equipped with a 30 kg-rated load cell with 1 g sensitivity (Texture Technologies Corp., Hamilton, MA). Compression was performed with a 4" diameter cylindrical probe operating at 0.5%/s strain rate up to a maximum compressional force of 2 N (<5% strain). Force data was recorded as a function of compressional distance in 1 μm increments, and sent to a PC for processing. Compression tests were repeated approximately 50 times over the subsequent 3-4 hours as the gelatin warmed, and the internal gelatin temperature was recorded with each test. The Young's modulus was calculated from the linear elastic region of each resulting stress-strain curve and is plotted as a function of temperature in Fig. 3 along with the cubic fit

$$E = 0.0026T^3 - 0.14T^2 + 1.0T + 24. \quad (19)$$

This fit allowed temperature to be used as a proxy for Young's modulus in Phantoms 1 and 2.

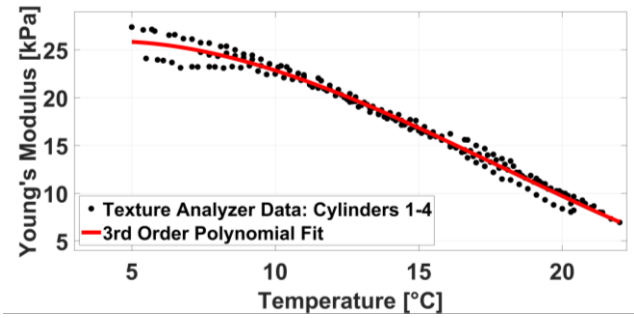

Fig. 3. Gelatin cylinder Young's moduli measured via compression testing as a function of internal temperature. The resulting polynomial fit (19) was used to convert measured temperatures to Young's moduli for Phantoms 1 and 2.

D. Inhomogeneous Magnetic Force Field Measurement

The magnetic field created by the solenoids in Fig. 2 lead to a spatially-inhomogeneous axial magnetic force in the ultrasound imaging area. Because the magnetic force was also modulated temporally, the spatial inhomogeneity of magnetic force *amplitude* was of central study. In order to characterize the axial magnetic force felt by one of the 0.5 mm diameter chrome steel ball bearings as a function of location, a "force sensing pendulum" was constructed.

As shown in Fig. 4, the force sensing pendulum was built around a 68 cm tall, ridged aluminum stand mounted on a 3-axis stage. A 4.9 mg 3D printed MicroFine™ pendulum bob (Proto Labs Inc, Maple Plain, MN, USA) held the magnetic ball internally, and was suspended via 40.5 cm of 0.1 mm diameter fishing line from the stand. The electromagnets were rotated 90 degrees relative to the orientation used for imaging such that the primary magnetic force axis (the axial direction) was horizontal rather than vertical. Thus, when current was applied to the magnets, the pendulum bob would equilibrate at a new location to the left of its original equilibrium position as shown in Fig.

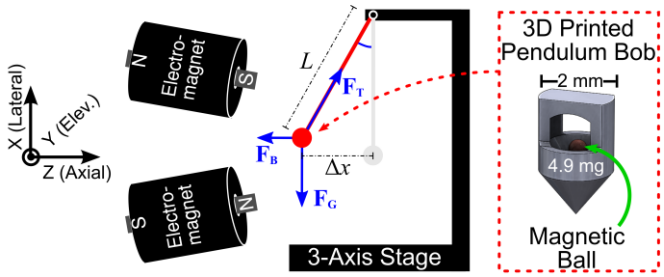

Fig. 4. Diagram of the force sensing pendulum. The electromagnets are rotated 90° relative to their usual position (see Fig. 2), and the magnetic ball inside a 3D printed pendulum bob is hung from a stand. When the magnets are turned on, the pendulum bob equilibrates to a new location. Given the horizontal deflection Δx, the weight of the ball and bob $\mathbf{F_G}$, and the length of the pendulum L, the magnetic force $\mathbf{F_B}$ at the ball's equilibrium location can be calculated. Values for different locations in the imaging area are obtained by adjusting the stage. Care is taken to ensure that the ball is always centered elevationally.

4. Given m, the combined mass of the pendulum bob, ball and the reduced mass of the string as well as the pendulum length L and horizontal displacement Δx, the magnetic force on the ball could be determined via

$$\mathrm{F}_B = mg\Delta x / L. \tag{20}$$

In order to measure horizontal displacement, a digital camera recorded video of the pendulum equilibrating, as a constant current of 12.6 A (the maximum available) was applied to the magnets over a 10 s time interval. A 1 mm grid placed behind the pendulum served as a reference, and video motion tracking was performed in Logger Pro (Vernier Software & Technology, Beaverton, OR, USA) to determine horizontal displacement. To minimize fluctuations from air currents the entire pendulum apparatus was enclosed in a clear acrylic box. The digital camera was positioned sufficiently far from the pendulum to minimize parallax.

The pendulum was used to make displacement measurements at 55 unique locations in the imaging area, and magnetic force was calculated at each. Measurements at different locations were achieved by moving the position of the magnets relative to the rest position of the pendulum using the 3-axis stage. In order to avoid unnecessary measurements, all data was collected for pendulum positions on one side of the axial centerline. Data was then mirrored across this centerline under the assumption that the magnetic force field was symmetric. As seen in Fig. 5a, a cubic interpolation was then applied to the data in order to generate the final force map.

In order to extend the utility of the force map to situations in which currents less than the maximum 12.6 A were supplied to the magnets, additional data was acquired at a single magnetic ball location. Nine force measurements at varying currents were made with the pendulum positioned on the axial centerline and 1.05 mm below the magnets. As can be seen in Fig. 5b, magnetic force amplitude increased as current increased, but two distinct linear regions were present, likely due to the onset of saturation in the magnet cores. Thus the conversion between current I (in Amperes) and magnetic force amplitude a (in μN) at a given location (x,z) was defined in a piecewise manner as

$$a(I,x,z) = \begin{cases} [0.15\,I - 0.078]\,a_{\max}(x,z), & I < 4.78\text{A} \\ [0.053\,I + 0.38]\,a_{\max}(x,z), & I \geq 4.78\text{A} \end{cases} \tag{21}$$

where $a_{\max}$ is the force amplitude (in μN) measured at the maximum 12.6 A current as plotted in Fig. 5a.

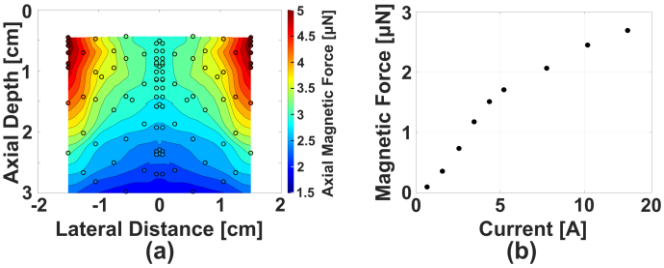

Fig. 5. Force map as measured by the force sensing pendulum. Plot (a) is a map of magnetic force as a function of position in the imaging area with magnet current set to its maximum value. Dots indicate measurements, and contours indicate a cubic interpolation. Plot (b) shows the magnetic force at one location as a function of current.

E. Validation Data Collection and Processing

In order to collect data on the MMUS signal as a function of axial magnetic force amplitude, Phantom 1 was used. The phantom was first removed from the refrigerator after overnight gelation, and then allowed to come to room temperature over a period of 3 hours. The phantom was placed into the MMUS imaging apparatus resulting in B-mode images such as the one seen in Fig. 6a. Magnetic force amplitude was varied by adjusting the peak current of the square-root sinusoidal waveform produced by the power supplies via the arbitrary waveform generator. Specifically, peak current was varied between 0 A, and the maximum value, 12.6 A, in ten roughly evenly-spaced steps. Eight images were collected at each current value for a total of 80 images. These data were collected in a random order to eliminate any potential time dependent effects, and phantom temperature was monitored throughout, and found to fluctuate no more than 0.5°C. Currents were converted to force amplitudes via (21), and (18) was used to produce the analytical model prediction for the MMUS signal of the magnetic ball in each image. For validation, the ball location was manually selected in each image, and a rectangle equivalent in size to one resolution cell was generated with its center coincident on the selected location. The displacement amplitude within that rectangular mask was averaged to produce the experimental MMUS signal for the magnetic ball.

Phantom 2 was used to collect data on the effect of gelatin Young's modulus and ball location within the inhomogeneous magnetic force field on MMUS signal. This phantom was removed from the refrigerator after overnight gelation, and then immediately subjected to imaging. The ultrasound transducer was positioned such that all three magnetic balls were centered elevationally, and MMUS images were collected over a timespan of 2.5 hours as the phantom warmed to room temperature. Because the gelatin warmed rapidly at first and then more slowly as the phantom approached room temperature, images were taken more frequently at the beginning. A total of 68 images were collected with 36 in the initial 45 minutes, and the rest spread out over the remaining 105 minutes. Temperatures were recorded for each image and converted to Young's moduli via (19). The model prediction and experimental MMUS signal for each of the three embedded magnetic balls was then determined as described previously.

IV. Results

Fig. 6c shows MMUS signal as a function of axial magnetic force amplitude for the single magnetic ball in Phantom 1. Each data point on the plot is the average signal from 8 images, and error bars represent the standard deviation. Temperature was held constant at 10.8 ± 0.2°C throughout. The model prediction for MMUS signal as given by (18) is shown as a solid blue line with the 95% confidence interval shaded light blue. As predicted by the model, the data demonstrate a strong linear dependence between force and displacement with $R^2 = 0.97$. All data points agree with the model within the confidence interval.

Figs. 7c and d show the model prediction and Phantom 2 validation results respectively for the Young's modulus dependence of MMUS signal. Each data point in Fig. 6d represents the average signal for a given ball over all images taken while the medium was within a 1 kPa range, and error bars correspond to the standard deviation. Weighted power law fits to the equation αE^{-1} where α corresponds to the coefficient in (18) are shown below the plots with 95% confidence intervals. As predicted by the model, balls 1-3 exhibit MMUS signals inversely proportional to Young's modulus, with R^2 values of 0.91, 0.68, and 0.88 respectively. The proportionality constants for Balls 2 and 3 agree within uncertainty.

V. Discussion and Future Work

The analytical model of magnetic particle displacement presented in (18) predicts that MMUS signal varies linearly with magnetic force amplitude, and inversely with medium Young's modulus. Experimental validation results corroborate both these functional dependencies as well as the signal magnitudes. As shown in Fig. 6c, varying the amplitude of the magnetic force while holding the phantom temperature, and thus Young's modulus, constant lead to a linear relationship between MMUS signal and force, with $R^2 = 0.97$. Furthermore, experimental MMUS signal magnitudes agree with the model for all 10 data points. As shown in Fig. 7d, each of the three magnetic balls in phantom 2 exhibit $1/E$-dependent MMUS signals with R^2 values of 0.91, 0.68, and 0.88. The overall MMUS signals were largest for ball 3 and smallest for ball 2. This means that the inhomogeneous force map given in Fig. 5 worked as expected as balls 3 and 2 were predicted to feel the largest and smallest magnetic force amplitudes, respectively. MMUS signal magnitudes agree with theory for balls 2 and 3, while exhibiting signals approximately 30% higher than theory for ball 1. As predicted by Fig. 1e, no transient behavior was observed in the experimental data. For the parameters used in this study, a transient decay time constant of less than 1 ms was expected, well below the $(2\ \text{Hz})^{-1}$ magnetic excitation period.

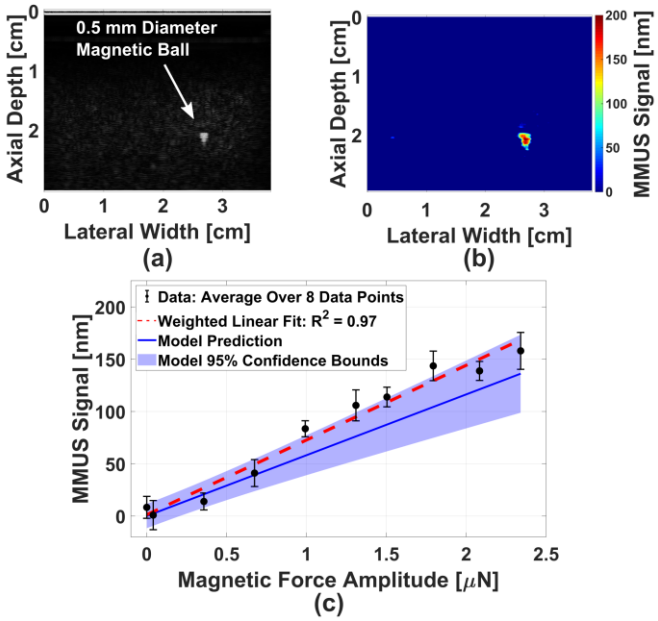

Fig. 6. Phantom 1 images and results: (a) Ultrasound B-mode image showing the location of the magnetic ball as a bright spot. (b) MMUS image showing the corresponding displacement map. Magnetically-induced displacement amplitude (*MMUS Signal*) is given by the color bar. (c) Average MMUS signal S in the resolution cell centered on the magnetic ball as a function of magnetic force amplitude a exhibits a linear relationship as predicted by (18). Error bars represent the standard deviation of repeated measurements.

A. Uncertainty Analysis

In order to establish agreement between model predictions and experimental data, it is important to understand the sources of uncertainty present, and how they affect the predicted MMUS signals. To determine the 95% confidence intervals displayed in Figs. 6 and 7, uncertainties in the ball radius R, the force amplitude a, and the medium Young's modulus E were propagated through equation (18).

Although different chrome steel magnetic balls from the same lot were used in each phantom, uncertainty in ball radius is unlikely to have contributed significantly to uncertainty in predicted MMUS signals. The manufacturer specified uncertainty is 0.003 mm, or 0.6%. When propagated to the displacement, the result is a contribution to MMUS signal

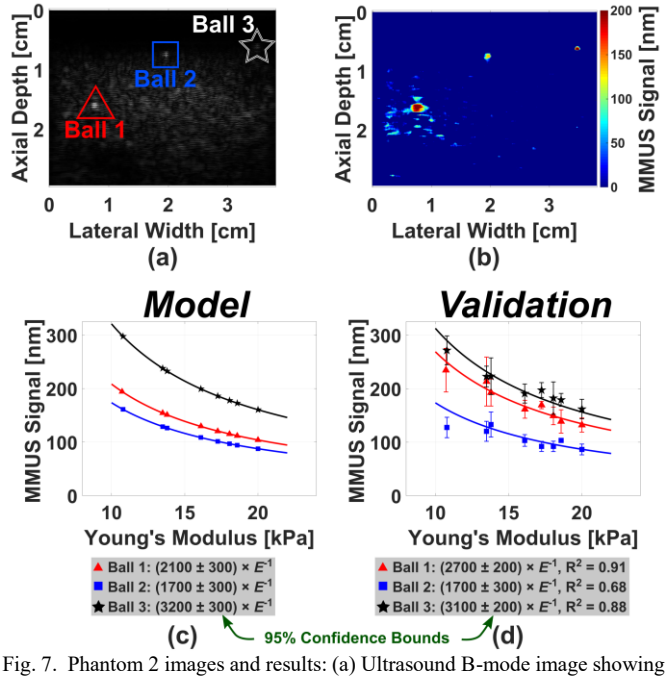

Fig. 7. Phantom 2 images and results: (a) Ultrasound B-mode image showing the locations of the magnetic balls. (b) Corresponding MMUS displacement map. Magnetically-induced displacement amplitude (*MMUS Signal*) is given by the color bar. (c) MMUS signal given by the model (18) as a function Young's modulus for forces corresponding to the ball locations in (a). (d) Experimental MMUS signals and weighted fits for balls 1-3 as a function of Young's modulus. Each data point is the average of all images within a 1 kPa range. Error bars represent the standard deviation.

variance of no more than 0.4%. Furthermore, an upper limit of 2% uncertainty in MMUS signal at high forces due to ball radius was confirmed in the lab, implying that ball radius does not have an important impact on overall uncertainty.

Uncertainty in the magnetic force amplitude measurements accounted for approximately 46% of the overall MMUS signal variance. Amplitudes were calculated based on physical parameters of the force sensing pendulum such as mass and length, as well as its rest and equilibrium positions when subjected to the magnetic driving force. These position measurements, which required manual frame-by-frame selection and suffered from a small parallax discrepancy as the pendulum bob moved out of line with the camera lens, contributed most to the overall uncertainties of approximately 0.2 μN. At higher force amplitudes, this propagates to only 3-10% uncertainty in MMUS signal. However, because different balls were used for the pendulum measurements and the phantoms, changes in the magnetic susceptibilities of the balls could potentially lead to additional uncertainty. Three precautionary measures were taken to avoid this. First, all chrome steel balls used in this work were taken from a single lot, second, all balls were passed through a demagnetizer before use, and third, plastic (rather than metal) tweezers were used at all times. To demonstrate agreement across balls, two phantoms prepared in the same manner as phantom 1 both exhibited average MMUS signals of 120±20 nm over the 8 images taken while each phantom had a Young's modulus of 13±2 kPa.

The largest contribution to uncertainty came from the Young's modulus measurement, which made up ~53% of the total variance in MMUS signal. In order to determine Young's moduli, thermocouples were embedded in the phantoms, and temperature measurements were converted to E via (19). The thermojunction was placed slightly away from the ball to avoid interference with imaging. Because warm air causes cold phantoms to warm from the outside in, thermocouples were buried at the same depth as were the magnetic balls. As an additional check, two separate thermocouples were embedded at similar depths within a block of gelatin. Temperature readings were monitored over 3 hours and never differed by more than 0.5°C, corresponding to a Young's modulus uncertainty of less than 1 kPa, or less than 20% of overall MMUS signal at higher force amplitudes. Uncertainty due to a temperature gradient causing a non-uniform Young's modulus during gelatin cylinder compression testing was reduced by using smaller volumes than in Phantoms 1 and 2, and was accounted for in the total variance.

B. *Contrast Agent Realism*

In this work, the magnetic contrast agent under study was chosen to be a chrome steel ball bearing with a known applied magnetic force in order to simplify the process of validating the model. Generally in MMUS imaging, magnetic nanoparticle contrast agents are used and the magnetically-induced motion of individual MNPs cannot be directly resolved due to their lack of echogenicity and ultrasound resolution constraints. It is instead the surrounding medium to which the particles are coupled that is imaged via MMUS. To match this situation, a low 1 MHz transmit and receive frequency was used so that the ball would be a sub-resolution target. MMUS signals were not observed to differ significantly when the transmit and receive frequencies were switched between 1 MHz and 10 MHz. Motion detected for any given resolution cell is a weighted average of motion within that cell, so while the scale was different, surrounding tissue motion was still taken into account. However, in order to extend the model for use with multiple particles, medium motion outside of a single resolution cell must be known. This may be achieved in the quasi-static limit by the solution to the displacement within an elastic solid, for example, as in [31]. Work in this group by Thapa *et al.* recently employed such a model to link the force on a distribution of MNPs to the resulting displacement field by employing Green's method[32]. Thapa's work provided medium displacements for a distribution of particles up to a scaling factor, while this work provided numerical values for displacements for a single particle. A combination of these two results may yield a quantitative, multi-particle model in future work. Furthermore, more work will be needed to assess the impact of nano-scale heterogeneities, such as porosity, in the medium surrounding MNPs.

Additionally, while the magnetic force applied to MNPs is not known for most MMUS systems, the model is still applicable. If the magnetic susceptibility of the MNPs and the magnetic gradient field in the imaging area are known, calculation of the force amplitude a should always be possible under the assumption of linear magnetization[33]. Future work may demonstrate that such measurements would obviate the need for the force sensing pendulum.

VI. Conclusion

In this study an analytical model for the motion of a single magnetic particle undergoing MMUS imaging was proposed. The model, based on a solution to the Navier-Stokes equation, assumed an infinite, homogeneous, linearly-elastic, and isotropic medium, with a single magnetic particle experiencing magnetically-induced displacement due to a spatially inhomogeneous and temporally sinusoidal driving force. The model was validated to exhibit similar functional dependencies with regard to the magnitude of the force and the medium Young's modulus. The model also quantitatively predicted displacement amplitudes within validation uncertainty. Thus, for any MMUS system, given either a magnetic force field or a magnetic gradient map and MNP susceptibility, the model may be used to predict the magnetically-induced motion under various medium conditions. This provides a method for verification of system performance as well as much-needed cross-system comparisons. For example, identical ball phantoms could be used to discriminate between signal losses due to different MNPs versus differences in the imaging apparatus. The model additionally provides a framework by which experimenters may design systems to either avoid or utilize resonant and transient displacements as desired.

ACKNOWLEDGMENT

B. E. Levy thanks J. B. Karlik for his contributions to the force sensing pendulum as well as Drs. S. Y. Emelianov and S. R. Aglyamov for their phantom preparation ideas and guidance.

REFERENCES

[1] S. Sjöstrand, M. Evertsson, and T. Jansson, "Magnetomotive Ultrasound Imaging Systems: Basic Principles and First Applications," *Ultrasound Med. Biol.*, vol. 46, no. 10, pp. 2636–2650, 2020.

[2] A. L. Oldenburg, J. R. Gunther, and S. A. Boppart, "Imaging magnetically labeled cells with magnetomotive optical coherence tomography.," *Opt. Lett.*, vol. 30, no. 7, pp. 747–749, 2005.

[3] J. Oh *et al.*, "Detection of magnetic nanoparticles in tissue using magneto-motive ultrasound," *Nanotech.*, vol. 17, no. 16, pp. 4183–90, 2006.

[4] A. G. Pope *et al.*, "Contrast-enhanced imaging of SPIO-labeled platelets using magnetomotive ultrasound," *Phys. Med. Biol.*, vol. 58, no. 20, pp. 7277–7290, Oct. 2013.

[5] M. Evertsson *et al.*, "Combined Magnetomotive ultrasound, PET/CT, and MR imaging of 68Ga-labelled superparamagnetic iron oxide nanoparticles in rat sentinel lymph nodes in vivo," *Sci. Rep.*, vol. 7, no. 1, pp. 1–9, 2017.

[6] M. Mehrmohammadi *et al.*, "In vivo pulsed magneto-motive ultrasound imaging using high-performance magnetoactive contrast nanoagents," *Nanoscale*, vol. 5, no. 22, p. 11179, 2013.

[7] S. Sjöstrand, "Contrast-enhanced magnetomotive ultrasound imaging (CE-MMUS) for colorectal cancer staging : Assessment of sensitivity and resolution to detect alterations in tissue stiffness," pp. 9–12, 2019.

[8] M. Fink, H. Ermert, C. Alexiou, and S. Lyer, "Detection of Iron Oxide Nanoparticles for Local Chemotherapeutic Treatment Employing Coded Magnetomotive Ultrasound," in *AMA Conferences Proceedings Sensor*, 2017, vol. C2-Acous, pp. 323–328.

[9] B. E. Levy, M. M. Hossain, J. M. Sierchio, D. Thapa, C. M. Gallippi, and A. L. Oldenburg, "Effect of model thrombus volume and elastic modulus on magnetomotive ultrasound signal under pulsatile flow," *IEEE Trans. Ultrason. Ferroelectr. Freq. Control*, vol. 65, no. 8, pp. 1380–1388, 2018.

[10] M. Holst *et al.*, "Phase-locked magnetomotive ultrasound imaging of superparamagnetic iron-oxide nanoparticles," *IEEE Int. Ultrason. Symp.*, pp. 1007–1010, 2010.

[11] M. C. Lu, J. Y. Houng, and M. L. Li, "Backward-mode ultrafast pulsed magnetomotive ultrasound," *IEEE Int. Ultrason. Symp.*, pp. 2–5, 2017.

[12] M. Mehrmohammadi, J. Oh, S. Mallidi, and S. Y. Emelianov, "Pulsed magneto-motive ultrasound imaging using ultrasmall magnetic nanoprobes," *Mol. Imaging*, vol. 10, no. 2, pp. 102–110, 2011.

[13] T. Ersepke, T. C. Kranemann, and G. Schmitz, "On the performance of time domain displacement estimators for magnetomotive ultrasound imaging," *IEEE Trans. Ultrason. Ferroelectr. Freq. Control*, vol. 66, no. 5, pp. 911–921, 2019.

[14] M. Evertsson *et al.*, "Revolving permanent magnet causes rotating particle motion that makes new detection schemes possible in magnetomotive ultrasound," *IEEE Int. Ultrason. Symp. IUS*, vol. 2019-Octob, pp. 2373–2375, 2019.

[15] M. Evertsson *et al.*, "Multimodal detection of iron oxide nanoparticles in rat lymph nodes using magnetomotive ultrasound imaging and magnetic resonance imaging," *IEEE Trans. Ultrason. Ferroelectr. Freq. Control*, vol. 61, no. 8, pp. 1276–1283, 2014.

[16] T. Ersepke, T. C. Kranemann, and G. Schmitz, "Frequency response of soft tissue displacements induced by the force on magnetic nanoparticles," Sep. 2017.

[17] T. Jansson *et al.*, "Induced tissue displacement in magnetomotive ultrasound imaging - Simulations and experiments," *IEEE Int. Ultrason. Symp. IUS*, pp. 639–642, 2014.

[18] M. Evertsson *et al.*, "Frequency- and phase-sensitive magnetomotive ultrasound imaging of superparamagnetic iron oxide nanoparticles," *IEEE Trans. Ultrason. Ferroelectr. Freq. Control*, vol. 60, no. 3, pp. 481–491, 2013.

[19] R. Andersson *et al.*, "Effect of nanoparticle size and magnetic field strength on the displacement signal in magnetomotive ultrasound imaging," *IEEE Int. Ultrason. Symp. IUS*, vol. 2016-Novem, 2016.

[20] S. Arsalani *et al.*, "The effect of magnetization of natural rubber latex-coated magnetite nanoparticles on shear wave dispersion magneto-motive ultrasound," *Phys. Med. Biol.*, vol. 64, no. 21, 2019.

[21] A. C. Bruno *et al.*, "Magnetomotive Ultrasound Elastography: Preliminary Evaluation in Phantom," *Brazilian Congr. Biomed. Eng.*, pp. 6–9, 2014.

[22] M. Fink, S. Lyer, C. Alexiou, S. J. Rupitsch, and H. Ermert, "Quantitative Imaging of the Iron-Oxide Nanoparticle- Concentration for Magnetic Drug Targeting Employing Inverse Magnetomotive Ultrasound," *Curr. Dir. Biomed. Eng.*, vol. 5, no. 1, pp. 417–419, 2019.

[23] T. C. Kranemann, T. Ersepke, S. Draack, and G. Schmitz, "Modeling and Measurement of the Nonlinear Force on Nanoparticles in Magnetomotive Techniques," *IEEE Trans. Ultrason. Ferroelectr. Freq. Control*, vol. 67, no. 4, pp. 679–690, 2019.

[24] M. Fink *et al.*, "Sonographic Detection of Magnetic Nanoparticles for Magnetic Drug Targeting Using Coded Magnetic Fields," *IEEE Int. Ultrason. Symp.*, vol. V, no. 1, pp. 1–6, 2015.

[25] M. M. Hossain, B. E. Levy, D. Thapa, A. L. Oldenburg, and C. M. Gallippi, "Blind Source Separation-Based Motion Detector for Imaging Super-Paramagnetic Iron Oxide (SPIO) Particles in Magnetomotive Ultrasound Imaging," *IEEE Trans. Med. Imaging*, vol. 37, no. 10, pp. 2356–2366, 2018.

[26] M. Fink, S. Lyer, C. Alexiou, and H. Ermert, "Sonographic detection of iron oxide nanoparticles employing shear waves," *Curr. Dir. Biomed. Eng.*, vol. 4, no. 1, pp. 457–459, 2018.

[27] O. Chaudhuri, J. Cooper-White, P. A. Janmey, D. J. Mooney, and V. B. Shenoy, "Effects of extracellular matrix viscoelasticity on cellular behaviour," *Nature*, vol. 584, no. 7822, pp. 535–546, 2020.

[28] Y. A. Ilinskii *et al.*, "Gas bubble and solid sphere motion in elastic media in response to acoustic radiation force," *J. Acoust. Soc. Am.*, vol. 117, no. 4, pp. 2338–2346, 2005.

[29] S. Chen, M. Fatemi, and J. F. Greenleaf, "Quantifying elasticity and viscosity from measurement of shear wave speed dispersion," *J. Acoust. Soc. Am.*, vol. 115, no. 6, pp. 2781–2785, 2004.

[30] E. L. Madsen *et al.*, "Tissue mimicking materials for ultrasound phantoms," *Medical Physics*, vol. 5, no. 5. pp. 391–394, 1978.

[31] S. Timoshenko and J. Goodier, *Theory of Elasticity*. McGraw-Hill, 1951.

[32] D. Thapa, B. E. Levy, D. L. Marks, and A. L. Oldenburg, "Inversion of displacement fields to quantify the magnetic particle distribution in homogeneous elastic media from magnetomotive ultrasound," *Phys. Med. Biol.*, vol. 64, no. 12, 2019.

[33] A. L. Oldenburg, F. J.-J. Toublan, K. S. Suslick, A. Wei, and S. A. Boppart, "Magnetomotive contrast for in vivo optical coherence tomography," *Opt. Express*, vol. 13, no. 17, p. 6597, 2005.

Benjamin E. Levy received his B.A. degree in Physics and Astronomy from Carleton College, Northfield, MN, USA, in 2015. He is currently a doctoral candidate in the Department of Physics and Astronomy at The University of North Carolina at Chapel Hill, USA. His interests include magnetomotive imaging, medical ultrasound research, and physics education.

Amy L. Oldenburg received the B.S. degree in applied physics from the California Institute of Technology in 1995 and the Ph.D. degree in physics from the University of Illinois at Urbana-Champaign in 2001.

Dr. Oldenburg performed postdoctoral work at the Beckman Institute at the University of Illinois at Urbana-Champaign where she invented magnetomotive OCT. In 2008 she founded the Coherence Imaging Laboratory at the University of North Carolina at Chapel Hill, where she is currently a Professor of Physics and Astronomy. Dr. Oldenburg received the NSF CAREER award in 2014. She became a Fellow of SPIE in 2019, and serves on the editorial board of the *Journal of Biomedical Optics*.